Running title: Modelling ECM dysfunction in haemorrhagic stroke

Adult organotypic brain slice cultures recapitulate extracellular matrix remodelling in haemorrhagic stroke

Benjamin J. Hewitt, PhD [1] – b.hewitt@bham.ac.uk
Lauren Roberts, BSc [2] **-** 129088318@aston.ac.uk
James A. Roberts, PhD [1] **–** j.roberts.6@bham.ac.uk
Daniel Fulton, PhD [3,4] **-** d.fulton@bham.ac.uk
Lisa J. Hill, PhD [1] - l.j.hill@bham.ac.uk
Phillip Kitchen, PhD [2] – p.kitchen1@aston.ac.uk
Roslyn M. Bill, PhD [2] – r.m.bill@aston.ac.uk
Hannah F. Botfield, PhD [3,4] – h.botfield@bham.ac.uk

[1] Department of Biomedical Sciences, School of Infection, Inflammation and Immunology, College of Medicine and Health, University of Birmingham, Birmingham, UK.

[2] Aston Institute for Membrane Excellence, Aston University, Birmingham, UK

[3] Inflammation and Ageing, School of Infection, Inflammation and Immunology, College of Medicine and Health, University of Birmingham, Birmingham, UK.

[4] Birmingham Centre for Neurogenetics, University of Birmingham, Birmingham, UK.

Corresponding authors:

Dr Benjamin Hewitt, PhD - Mailing address: Neuroscience and Ophthalmology, Robert Aitken Institute for Clinical Research, University of Birmingham, Birmingham, B15 2PA, United Kingdom. Tel: +44(0)121 414 8859

Dr Hannah Botfield, PhD - Mailing address: Neuroscience and Ophthalmology, Robert Aitken Institute for Clinical Research, University of Birmingham, Birmingham, B15 2PA, United Kingdom.

Running title: Modelling ECM dysfunction in haemorrhagic stroke

1. Abstract

Haemorrhagic stroke is a devastating condition characterised by vessel rupture and free blood within the brain parenchyma or cerebrospinal fluid (CSF) filled spaces. Across the major subtypes of haemorrhagic stroke (subarachnoid, intracerebral, and intraventricular haemorrhages), the presence of blood in the CSF generates significant tissue damage in the first 72 hours after the event, known as early brain injury (EBI). EBI includes neuroinflammation, blood-brain barrier breakdown and dysregulation of extracellular matrix (ECM) dynamics. ECM dysfunction has been shown to trigger fibrosis of the cortical blood vessels, limiting normal CSF circulation and resulting in the buildup of metabolic waste or the development of post-haemorrhagic hydrocephalus. Limiting or preventing this fibrosis may therefore reduce the rate of morbidity experienced by survivors, providing a potential avenue for non-surgical treatment to reduce secondary brain injury post-stroke.

Despite this, current *in vivo* approaches fail to differentiate between the effect of blood products and secondary consequences including intracranial pressure (ICP) elevation and mass effect. Here, we describe an adult rat organotypic brain slice culture (OBSC) model of haemorrhagic stroke which enables the identification of the effect of blood products on ECM dysregulation. We demonstrate the distribution of key cell types across a time course of 0, 3 and 7 days in culture, indicating that such cultures are viable for a minimum of 7 days. Using immunofluorescence staining, Western blotting and RNA sequencing, we show that exposure of OBSCs to lysed blood markedly increases ECM deposition around cortical blood vessels. This is accompanied by dysregulation of ECM regulatory genes and upregulation of inflammation and oxidative stress-related genes, successfully recapitulating the changes seen in human stroke survivors. This versatile *ex vivo* model provides a translational platform to further understanding of haemorrhagic stroke pathophysiology and develop or trial novel therapeutics prior to progression to *in vivo* stroke studies.

2. Introduction

Haemorrhagic stroke is a devastating condition characterised by vessel rupture and free blood within the brain parenchyma or cerebrospinal fluid (CSF)-filled spaces, and may be split into intracerebral haemorrhage, subarachnoid haemorrhage (SAH) and intraventricular haemorrhage depending on the location of the bleed. While haemorrhagic stroke only accounts for approximately 20% of stroke cases [1], the risk of mortality or profound disability is markedly greater than that posed by ischemic stroke [2].

SAH is most commonly triggered by a ruptured aneurysm causing blood to leak into the CSF in the subarachnoid space, with blood also entering the ventricles in higher grade SAH. Early brain injury (EBI) is the injury that occurs in the brain within 72 hours of an SAH and develops due to mechanical factors and the direct effect of free blood. SAH causes an increase in intracranial pressure (ICP), decreased cerebral blood flow (resulting in global ischemia), blood brain barrier (BBB) breakdown, brain oedema, oxidative stress and neuroinflammation, which ultimately leads to neurodegeneration [3].

Extracellular matrix (ECM) dynamics in and around the brain are also affected following SAH. There is a fine balance between ECM deposition and degradation which is particularly evident within blood vessel architecture. Under pathological conditions, BBB dysfunction is associated with the degradation of ECM in the basement membrane, mainly through matrix metalloproteinases. This can then release growth factors such as the pleiotropic cytokine transforming growth factor-β1 (TGF-β1) which in turn stimulates vascular smooth muscle cells (SMCs) to promote ECM deposition and repair the BBB [4]. SAH can result in excessive or dysregulated ECM deposition around major blood vessels on the surface of the brain, contributing to the development of cerebral vasospasm and subsequent delayed cerebral ischemia [4]. Furthermore, elevated TGF-β1 levels have been implicated in the development of subarachnoid fibrosis and ECM dysfunction in CSF drainage pathways after SAH which can

lead to the development of post-haemorrhagic hydrocephalus [5–8]. Understanding the pathways and mechanisms involved in ECM dysfunction may provide therapeutic targets for reducing further brain injury following SAH.

In both human patients and animal models of SAH, it can be difficult to differentiate between the response of the brain to the mechanical factors that follow a stroke (ICP elevation, mass effect) and the direct reaction of brain tissue to blood products, which is important to understand the pathogenesis of common sequalae to SAH and focus the development of future therapeutics to treat these. In contrast, *ex vivo* models allow us to differentiate between these factors to identity and further understand disease processes. Organotypic brain slices cultures (OBSCs), which were first described in the 1950s for the study of membrane potentials in the cerebral cortex [9], have been used in the study of neurodegenerative diseases [10], invasive glioma [11] and epilepsy [12] amongst many other uses. OBSCs provide a three-dimensional tissue architecture and are widely considered to be more representative of the *in vivo* state than cell cultures due to the presence of neurons, glial cells and endothelial cells in a native tissue architecture [13]. OBSCs are typically prepared from neonatal brain tissues slices as these tend to be more resistant to the mechanical trauma caused by sectioning, making them easier to culture [14]. However, these neonatal models are unlikely to recapitulate the complexity or maturity of adult tissues, as is shown by different responses to sectioning. For this reason, adult OBSC models are essential in modelling a disease which primarily affects middle to older-aged adults [15]. Whilst adult rodent OBSCs are now well established, there has been very limited prior exploration of their application to haemorrhagic stroke research. Attempts at short-term (minutes to hours) haemorrhagic stroke brain slice models have been reported with a focus on neuronal survival, though it is not clear whether they were from adult or neonatal animals [16]. Therefore, the development and validation of an adult OBSC system capable of modelling haemorrhagic stroke remains an important challenge.

Here, we describe the generation and validation of OBSCs derived from healthy adult rats and their application to the *ex vivo* modelling of post-haemorrhagic stroke ECM dysfunction and inflammation. *Ex vivo* recapitulation of ECM dynamics may provide an opportunity for furthering understanding of the molecular mechanisms underlying this key factor in post-stroke brain injury and offer a platform in which to trial novel therapeutics prior to use *in vivo*.

108 # 3. Methods

109 ## 3.1. Tissue culture

110 All tissue culture was performed under aseptic conditions using a class II microbiological
111 safety cabinet (Monmouth Guardian T1200). Tissues were cultured at 37°C, 5% CO_2 and
112 100% relative humidity.

113 Dissection media for OBSC generation comprised Earle's balanced salt solution
114 supplemented to a final concentration of 25 mM HEPES. OBSC culture media comprised 1:1
115 Dulbecco's Modified Eagle Media (DMEM):Neurobasal A, supplemented with final
116 concentrations of 2% (v/v) B-27, 2 mM L-glutamine and 1% penicillin/streptomycin solution.

117 ## 3.2. Experimental animals

118 Male Sprague-Dawley rats were group housed with access to food and water *ad libitum*, on a
119 12-hour light/dark cycle. All studies were conducted at the University of Birmingham, and
120 both the establishment and investigators held relevant UK Home Office licenses. Animals
121 were monitored daily and group housed, with no regulated procedures performed. Animals
122 were euthanized according to Schedule 1 of the Animals (Scientific Procedures) Act 1986 at a
123 weight of 130-150 g by intraperitoneal injection of 200 mg/ml pentobarbitol, 4 ml/kg and
124 decapitated following cessation of circulation. Blood was captured in a sterile, un-heparinised
125 50 ml centrifuge tube and stored at -20°C until required.

126 ## 3.3. Organotypic brain slice culture (OBSC) generation

127 The brain was rapidly removed from the skull and the cerebellum and olfactory bulbs excised
128 with a sterile scalpel. A flat face was produced on the rostral and caudal edges of the brain by
129 cutting (Figure 1), and the brain adhered to the chuck of a vibratome (7000smz, Campden

130 Instruments) (caudal side down) with cyanoacrylate glue. The brain was then mounted into
131 the vibratome bath, containing 250 ml dissection medium on ice, bubbled with medical
132 oxygen at 2 psi. 250 µM sections were produced with the vibratome set to a 1.25 mm
133 amplitude at 80 Hz and sections stored in the dissection media bath until completion.

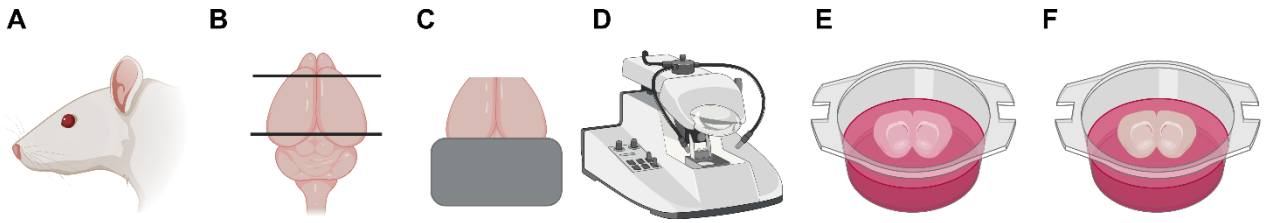

134

135 **Figure 1 – Steps in the generation of adult rat brain OBSCs.** A) Sacrifice and brain
136 removal, B) Removal of olfactory bulbs and cerebellum, including production of a flat edge
137 on the caudal aspect of the cerebrum, C) Mounting of brain (caudal face down) onto
138 vibratome chuck with cyanoacrylate glue, D) Vibratome slicing of brain (250 µM sections, 80
139 Hz, 1.25 mm amplitude), E) Brain slices added to 6-well cell culture inserts, F) Media
140 removed to bring brain slice to air-liquid interface.

141

142 Slices were then transferred to 6-well polyethylene culture inserts (657641, Greiner) using a
143 fine paintbrush and spatula. To facilitate this, 1 ml of culture medium was initially added to
144 each insert to enable floating of the slice, which was removed once the slice was correctly
145 positioned. Culture inserts were added to a standard 6-well plate (3516, Corning), and 1.5 ml
146 of OBSC culture medium added to the bottom well with the top insert containing the brain
147 slice left dry. Slices were then either fixed immediately or on day in-vitro (DIV) 3 or 7 using
148 4% paraformaldehyde (PFA) in PBS for one hour at room temperature, followed by two, one-
149 hour phosphate buffered saline (PBS) washes at room temperature prior to storage in PBS at
150 4°C.

151 **3.4. Blood-treated OBSCs**

152 OBSCs destined for blood treatment as a model of haemorrhagic stroke were generated as
153 described above and exposed to blood immediately or after 7 days of pre-culture.

154 Blood from all animals was pooled, vortexed and shaken vigorously to break up clots, and
155 diluted 1:1 with PBS. 6, 24 or 48 hours prior to the experiment endpoint, 175 µl of diluted
156 blood (or PBS control) was added to the wells assigned for blood treatment after removal of
157 an equal volume of medium. Brain slices for immunohistochemical analysis were then fixed
158 as previously described, prior to washing through two changes of PBS and storage at 4°C.

159 Slices destined for protein or RNA extraction were dissected under a surgical microscope,
160 with the cortex removed (taking care to avoid capturing any tissue from the corpus callosum),
161 snap frozen in liquid nitrogen and stored at -80°C.

162 **3.5. Immunohistochemical staining and imaging**

163 OBSCs were divided into two hemispheres prior to staining. A full protocol for staining and
164 clearing of OSBCs can be found in the supplemental materials ('Staining and clearing of
165 OBSCs'). Antibodies were diluted in PBS with 0.2% (v/v) triton X-100, 6% (v/v) goat serum
166 and 20% (v/v) DMSO, with 0.2 ml of diluted antibody added to each slice in a 24-well plate.
167 Imaging was performed using an AxioScan Z.1 (Zeiss) for blood exposed sections and an
168 AxioScan 7 (Zeiss) for timepoint studies maintaining the same imaging settings across all
169 slides within an analysis group. 4,6-diamidino-2-phenylindole (DAPI) was included at a
170 1:5000 dilution of a 5 mg/ml stock in PBS.

171

172 **Table 1 – Antibody dilutions used in immunofluorescent staining of OBSCs.**

Antibody	Dilution
Anti-rat endothelial cell antigen 1 (RECA-1), mouse	1:100
Anti-fibronectin, rabbit	1:400
Anti-alpha smooth muscle actin (αSMA), mouse	1:500
Anti-cleaved caspase 3 (CCP3), rabbit	1:500
Anti-NeuN, mouse	1:500
Anti-GFAP, mouse	1:400
Anti-collagen IV, rabbit	1:500
Anti-IBA1, rabbit	1:500
AF488 conjugated anti-rabbit IgG, highly cross-absorbed	1:1000
AF594 conjugated anti-mouse IgG, highly cross-absorbed	1:1000

173

174 **3.6. Image processing and analysis**

175 Image processing was performed using FIJI [17], with the operator blinded to the treatment or
176 culture conditions of each image by displaying only numerical filenames. Representative
177 images shown have been enhanced for display by modification of window and level,
178 performed uniformly across all images within a comparison group or stain. No image
179 enhancement was performed on images prior to image analysis.

180 Images were processed using a FIJI macro [17], made available both on GitHub
181 (https://github.com/Dr-ben-hewitt/OBSC-quantification-macros) and in the supplementary
182 materials. In brief, this performed a maximum intensity projection and presented the user
183 with an image in the red channel only (corresponding to blood vessel staining with RECA-1).
184 Five regions of interest (ROIs) were then manually selected in the cortex of each slice and

185 processed for background subtraction (100 pixel radius for RECA-1 channel, 1000 pixel
186 radius for fibronectin and collagen IV), followed by automatic thresholding of blood vessels
187 (RenyiEntropy method) and ECM proteins (Triangle method), with image calculation then
188 performed to find the average of these two sets of features.

189 Mean pixel intensity per unit area was calculated by user selection of 3 ROIs per image (with
190 the user shown only the DAPI channel to limit bias), followed by background subtraction (50
191 pixel radius) in FIJI, automated measurement of the integrated ROI pixel intensity and
192 division of this value by the area of the ROI.

193 **3.7. <u>Protein extraction and Western blotting</u>**

194 Protein extraction was performed by mechanical homogenisation in 250 µl
195 radioimmunoprecipitation assay (RIPA) buffer, supplemented with protease and phosphatase
196 inhibitors per manufacturers guidance. Samples were then incubated on a roller at 4°C for 2
197 hours and centrifuged at 10,000×*g* for 20 minutes at 4°C. Supernatant was then harvested,
198 aliquoted and stored at -80°C until required. Protein concentration was assessed by BCA
199 assay, following the manufacturer's instructions. SDS-PAGE was performed using 2.5 µg of
200 protein in a 20 µl volume, containing 5 µl LDS sample buffer and 2 µl reducing agent, on 4-
201 12% bis-tris polyacrylamide gels using MOPS-SDS running buffer. Electrophoresis was
202 performed at 120 V for 90 minutes. Proteins were then transferred to a nitrocellulose
203 membrane using NuPAGE transfer buffer at 25 V for 1 hour. Blocking was performed by
204 immersion in 5% (w/v) skimmed milk in tris-buffered saline with 0.1% (v/v) Tween-20
205 (TBST) for one hour at room temperature. Blots were then incubated in primary antibodies
206 for fibronectin or collagen IV and alpha-actin diluted in blocking buffer for one hour at room
207 temperature, washed three times in TBST (15 minutes each, room temperature), and
208 incubated in secondary antibody (1:5000 anti-IgG HRP conjugated) for one hour at room

209 temperature. Blots were then washed 3x in TBST (10 minutes each, room temperature) prior
210 to immersion in chemiluminescent substrate for 5 minutes (room temperature) and imaging
211 (G:Box chemi XRQ, Syngene).

212 **3.8. RNA extraction, sequencing and RT-qPCR**

213 Samples were mechanically disrupted and homogenised in 1 ml TRIzol and 200 µl
214 chloroform was then added. Samples were then mixed by shaking and centrifuged at
215 12,000*g* for 15 minutes at 4°C. The upper aqueous phase was removed and transferred to a
216 new tube, and an equal volume of molecular grade 70% ethanol added. RNA was then
217 extracted from the sample with an RNEasy mini extraction kit (Qiagen), following the
218 manufacturer's instructions for a 40 µl elution volume in RNase free water. RNA was then
219 quantified by spectrophotometery (N50 NanoPhotometer, Implen). Sample quality control
220 (integrity, purity and concentration via Agilent 5400) and paired-end mRNA sequencing was
221 performed by a contracted 3rd party (Novogene, UK) using a NovaSeq X Plus (Illumina) at a
222 read depth of 20 million reads per sample.

223 Alignment against a Sprague Dawley rat genome (rn_celera) was performed by Novogene,
224 followed by mapping to the same reference genome using the featureCounts tool [18] on the
225 Galaxy platform [19], followed by quality control using MultiQC [20]. Analysis of differentially
226 expressed genes was performed with DESeq2 [21], with comparisons made of expression in
227 blood-treated samples against an untreated control. Differentially expressed genes were
228 defined as those with an adjusted p-value (*pAdj)* < 0.05, and a fold change cutoff of 2 was
229 used for display of DEGs.

230 Gene ontology (GO) analysis was performed on all differentially expressed genes (with no
231 fold-change cutoff) using goseq [22], with gene categories retrieved from the rn6 assembly due

232 to unavailability of gene categories for the rn_celera assembly. All visualisation of RNA-
233 sequencing data was performed using GraphPad Prism 10.3.

234 Validation of the top 6 most upregulated and top 6 most downregulated genes was performed
235 using RT-qPCR. In brief, cDNA conversion was performed with a Tetro cDNA kit using
236 Oligo(dT)18 primers and 100 ng of RNA. cDNA was then further diluted by addition of 20 µl
237 molecular biology grade water. RT-qPCR mastermix comprised 100 µl SYBR green, 78 µl
238 water and 1 µl of each forward and reverse primer (reconstituted to 100 µM). 9 µl mastermix
239 was added to each well of a 384-well PCR plate, followed by 1 µl cDNA. RT-qPCR was
240 performed using a QuantStudio 5, with reaction conditions shown in supplemental materials
241 **Error! Reference source not found.**1. Oligonucleotide primers used are shown in
242 supplemental materials Table S2

243

244 **3.9. <u>Statistical analysis</u>**

245 All statistical analysis was performed in GraphPad Prism 10.3, with a significance level of
246 0.05. Statistical tests are described in the relevant figure legends.

247 RT-qPCR data were analysed with QBase+ (Biogazelle, Belgium) using the calibrated
248 normalised relative quantity (CNRQ) method. Four housekeeping genes were assessed using
249 the geNorm algorithm within QBase+ and the two housekeeping genes with lowest mean
250 variability were used as reference genes for sample normalisation.

251 **3.10. <u>Key resources table</u>**

REAGENT or RESOURCE	SOURCE	IDENTIFIER
Antibodies		

Anti-rat endothelial cell antigen 1 (RECA-1), mouse	Abcam	CAT# Ab9774
Anti-fibronectin, rabbit	Invitrogen	CAT# F3648
Anti-alpha smooth muscle actin (αSMA), mouse	ThermoFisher	CAT# 14-9760-82
Anti-cleaved caspase 3 (CCP3), rabbit	Cell Signalling Technologies	CAT# CST96615
Anti-NeuN, mouse	Cell Signalling Technologies	CAT# 94403
Anti-GFAP, mouse	Sigma	CAT# G3893
Anti-collagen IV, rabbit	BioRad	CAT# 2150-1470
Anti-IBA1, rabbit	FujiFilm Wako	CAT# 019-19741
AF488 conjugated anti-rabbit IgG, highly cross-absorbed	ThermoFisher	CAT# A32731
AF594 conjugated anti-mouse IgG, highly cross-absorbed	ThermoFisher	CAT# A32742
Anti-alpha-actin	Abcam	CAT# Ab179467
Anti-IgG HRP conjugated	Abcam	CAT# Ab6721
Chemicals, Peptides and Recombinant Proteins		
Earle's balanced salt solution	Gibco	CAT# 11540616
HEPES	Fisher Scientific	CAT# 10204932
DMEM cell culture medium	Fisher Scientific	CAT# 11965092
Neurobasal A	Fisher Scientific	CAT# 11540366
B-27	Fisher Scientific	CAT# 11530536
L-glutamine	ThermoFisher	CAT# 25030024
Penicillin-Streptomycin	ThermoFisher	CAT# 15070063
Pentoject, Pentobarbital sodium	Animalcare	CAT# XVD132
Cyanoacrylate glue	RS	CAT# 835-4131
Paraformaldehyde	Merck	CAT# 47608-1L-F
Phosphate Buffered Saline (PBS) tablets	Fisher Scientific	CAT# 10209252
Triton X-100	Merck	CAT#X100-1GA
Goat serum	Fisher Scientific	CAT# 11530526
4′,6-diamidino-2-phenylindole (DAPI)	Invitrogen	CAT# D21490
Radioimmunoprecipitation assay (RIPA) buffer	ThermoFisher	CAT# 89900
cOmplete™ Protease Inhibitor Cocktail	Roche	CAT# 11697498001
PhosSTOP™ Phosphatase Inhibitor	Roche	CAT# 4906845001
Lithium Dodecyl Sulfate (LDS) buffer	ThermoFisher	CAT# NP0007

Sample Reducing Agent	ThermoFisher	CAT# NP0004
Bis-Tris Mini Protein Gels, 4–12%	ThermoFisher	CAT# NP0322
MOPS SDS Running Buffer	ThermoFisher	CAT# NP0001
Protran 0.45 NC nitrocellulose Western blotting membranes	Cytiva	CAT# 10600007
NuPAGE™ Transfer Buffer	ThermoFisher	CAT# NP00061
Skimmed milk powder	VWR	CAT#84615.0500
Tris-buffered saline	Merck	CAT#524750
Tween20	Scientific Laboratory Supplies	CAT#CHE3852
SuperSignal™ West Pico PLUS Chemiluminescent Substrate	ThermoFisher	CAT# 34580
TRIzol	Invitrogen	CAT# 12044977
Chloroform	ThermoFisher	CAT# J67241.K2
Molecular grade ethanol	Fisher Scientific	CAT#BP2818-212
RNase-Free Water	Qiagen	CAT# 129112
Nuclease-Free Water	Qiagen	CAT# 129117
SYBR™ Green Universal Master Mix	ThermoFisher	CAT# 43-091-55
Critical Commercial Assays		
Bicinchoninic Acid (BCA) Assay Kit	ThermoFisher	CAT# 23225
RNeasy Mini Kit	Qiagen	CAT# 74104
Tetro™ cDNA Synthesis Kit	Bioline	CAT# BIO65043
Experimental Models: Organisms/Strains		
Sprague-Dawley rat	Inotiv	CAT# 002
Oligonucleotides		
Primers for quantitative reverse-transcription PCR (RT-qPCR)	Supplemental materials Table S2	Supplemental materials Table S2
Software and Algorithms		
FIJI	FIJI	https://fiji.sc/
Image processing macro: Percentage coverage of blood vessels	This paper	https://github.com/Dr-ben-hewitt/OBSC-quantification-macros
Image processing macro: Intensity per unit area	This paper	https://github.com/Dr-ben-hewitt/OBSC-quantification-macros
Galaxy	Galaxy	https://usegalaxy.org/
GraphPad Prism 10.3	Graphpad	https://www.graphpad.com/scientific-software/prism
QBase+	CellCarta	https://cellcarta.com/genomic-data-analysis/

Zen 3.1	Zeiss	https://www.zeiss.com/microscopy/en/products/software/zeiss-zen.html
GeneSys / GeneTools	SynGene	https://www.syngene.com/software/

4. Results

4.1. Health of the OBSCs after 7 days in culture

Cleaved caspase-3 (CPP3) staining was used as a marker of apoptosis. Overall, there was an increase in CCP3-positive staining from DIV0 to DIV7 in the cortex (Figure 2A) and other areas of the OBSC (Figure S3). Quantification of the mean CCP3-positive pixel intensity per unit area revealed a significant increase in CCP3 signal in the cortex (Figure 2B), increasing from 1.21×10^{-6} at 0 days to 2.04×10^{-6} at 3 days ($P = 0.0081$) and 2.72×10^{-6} at 7 days ($P = 0.0001$). A significant increase in CCP3 signal between DIV0 and DIV7 was also noted in the basal ganglia (Figure S3).

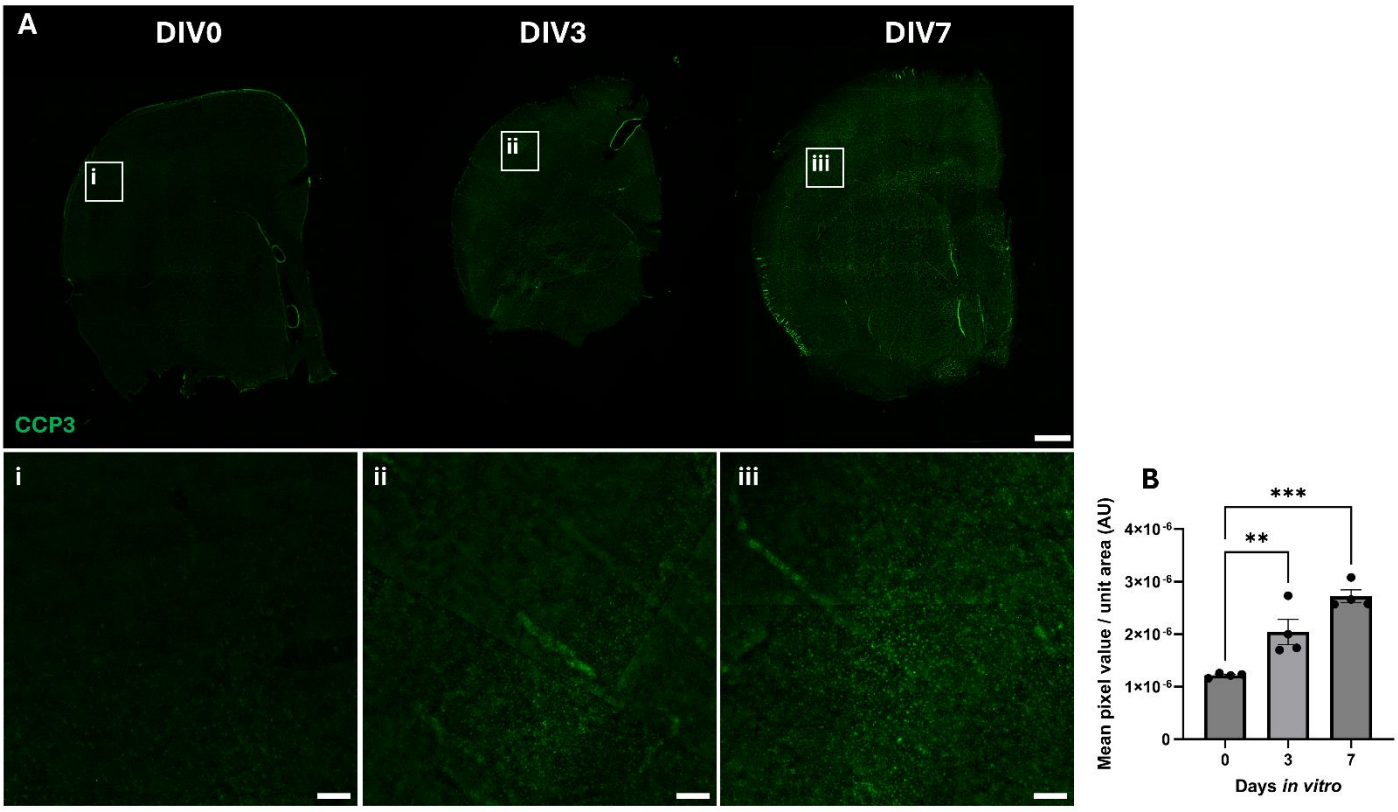

Figure 2 – Distribution and intensity of CCP3 throughout control and cultured OBSCs.

A) Representative immunofluorescent staining of OBSCs (CCP3, green and DAPI, blue) at 0 3 and 7 days *in vitro* (scale bar = 1,000 µm). Magnified regions of the cortex of section are shown in insets 'i', 'ii' and 'iii' for DIV0, 3 and 7 respectively (scale bar = 100 µm for all). Quantification of mean CCP3-stained pixel intensity per unit area in the cortex was also performed (B). Each image quantification datapoint is mean of 6 regions of interest from 2 brain slices per animal (3 regions per slice), ± SEM. One-way ANOVA with Dunnett's multiple comparisons test (all to all). ns = not significant, ** $P < 0.01$, *** $P < 0.001$. $N = 4$ animals, $\alpha = 0.05$.

4.2. Alterations in the organotypic cytoarchitecture of the cortex after 7 days in culture

Previous studies suggested OBSCs need to be cultured for 7-14 days prior to use in order to allow the slices to recover from the trauma of vibratome sectioning. Therefore, the cellular composition of OBSCs was assessed at DIV0, DIV3 and DIV7.

NeuN, a neuronal cell marker, demonstrated stable levels in the cortex of OBSCs at DIV0, DIV3 and DIV7 (Figure 3A), with no significant differences observed in NeuN staining intensity between DIV0 (mean pixel intensity per unit area of 1.21×10^{-5}) and DIV3 or 7 (8.49×10^{-6} and 6.24×10^{-6} respectively, Figure 3B). In the cortex, glial fibrillary acidic protein (GFAP)-positive astrocytes (Figure 3C) appeared to show a marked reduction in staining from DIV0 to DIV7, particularly with a loss in the glia limitans. This was further supported by a significant reduction in quantified GFAP mean pixel value at both DIV3 and DIV7 compared to DIV0. Mean pixel intensity per area of GFAP was reduced by more than 50% from 5.3×10^{-6} at DIV0 to 2.0×10^{-6} and 2.5×10^{-6} at DIV3 and DIV7 ($P < 0.0001$ and $P = 0.0001$, respectively) (Figure 3D). In contrast, GFAP-positive astrocytes were maintained within the deeper subcortical white matter (supplemental materials, Figure S4).

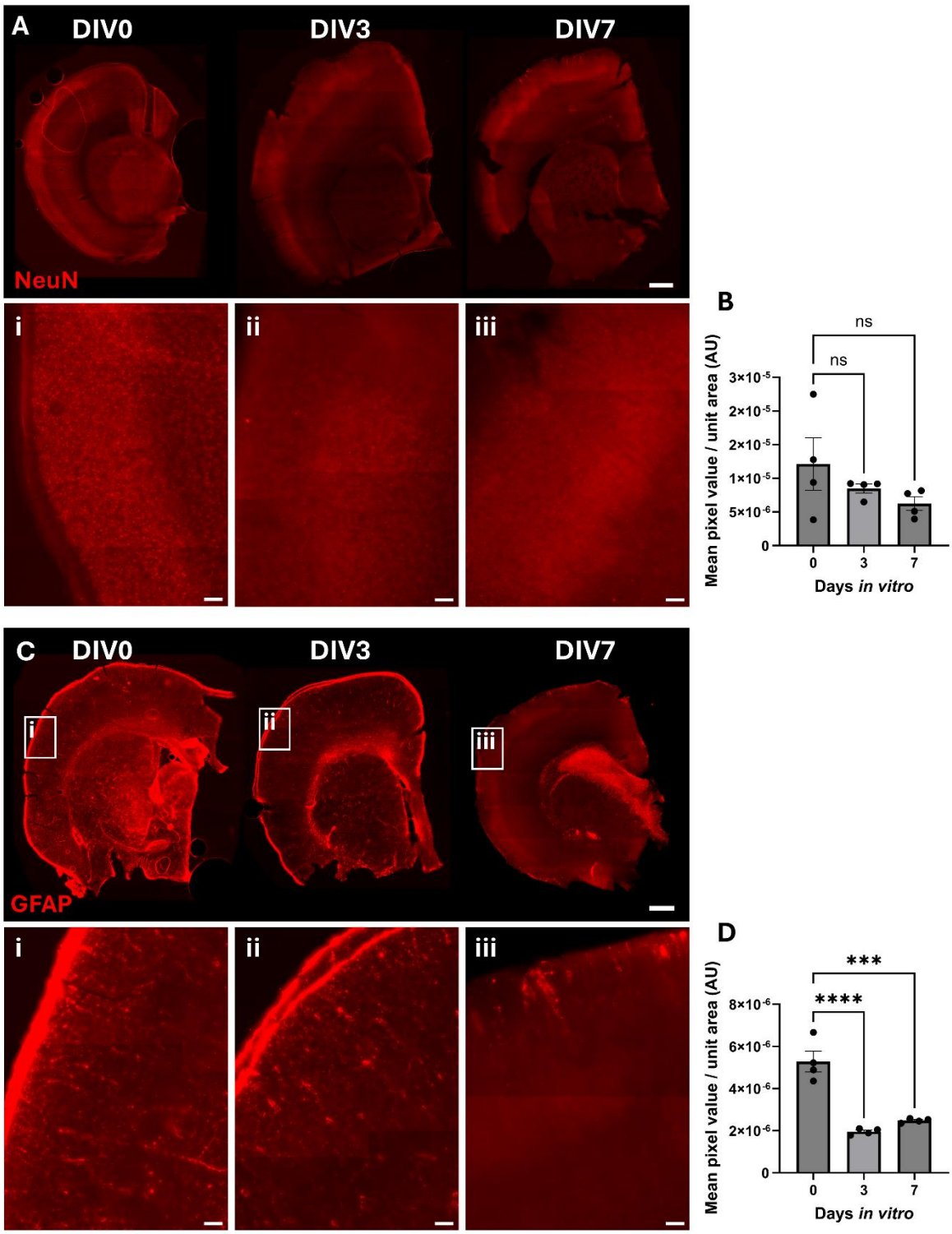

Figure 3 - Immunofluorescent staining of neurons and astrocytes in OBSCs after 0, 3 and 7 days *in* vitro (DIV). Representative immunofluorescent staining of A) NeuN (neuronal cell marker) and C) GFAP (astrocyte marker) shown in red, with DAPI nuclear counterstain in blue (scale bars = 1,000 µm). Magnified regions of the cortex of section are shown in insets 'i', 'ii' and 'iii' for DIV0, 3 and 7 respectively (scale bars = 100 µm in insets), in addition to quantification of the mean pixel value per unit area for these regions in insets B) NeuN quantification in cortex, D) GFAP quantification in cortex. Each datapoint is

the mean of 3 regions of interest per brain slice, ±SEM. All statistics were performed with one-way ANOVA with Dunnett's multiple comparisons test (all to control). ns = not significant, ** $P < 0.01$, *** $P < 0.001$, **** $P < 0.0001$. $N = 4$ animals, $\alpha = 0.05$.

Ionized calcium-binding adapter molecule 1 (IBA1) was used as a microglial cell marker. There was a reduction in IBA1-positive cells in the cortex in DIV3 and DIV7 compared to DIV0 (Figure 4A). Image analysis showed a significant reduction after 3 and 7 days of culture, from a mean IBA1 pixel intensity per unit area of 4.87×10^{-6} at DIV0 to 1.69×10^{-6} at DIV3 and 1.63×10^{-6} at DIV7 (Figure 4B, $P = 0.0150$ and 0.0134 respectively). However, similar to GFAP staining, there did not appear to be any significant changes in IBA1 staining in the subcortical white matter (Figure S4).

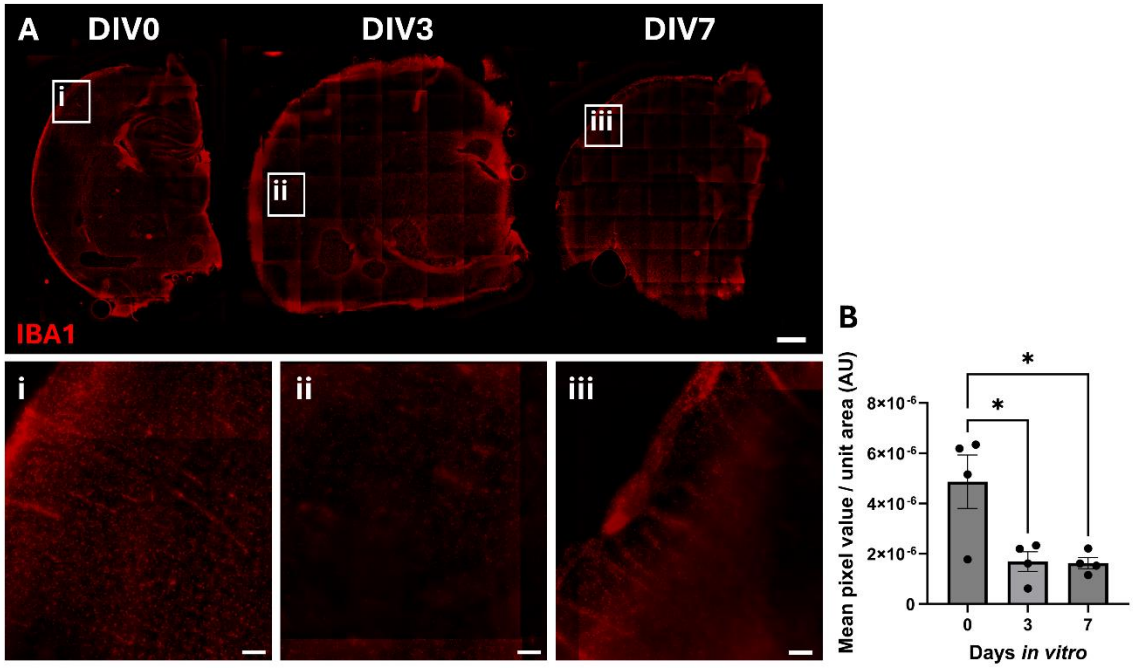

Figure 4 - Immunofluorescent staining of microglia in OBSCs after 0, 3 and 7 days *in vitro* (DIV). Representative immunofluorescent staining of IBA1 shown in red (scale bars = 1000 µm). Magnified regions of the cortex of section are shown in insets 'i', 'ii' and 'iii' for DIV0, 3 and 7 respectively, in addition to quantification of the mean pixel value per unit area (scale bars = 100 µm in insets). Each datapoint is the mean of 3 regions of interest per brain slice, ±SEM. All statistics were performed with one-way ANOVA with Dunnett's multiple comparisons test (all to control). ns = not significant, * $P < 0.05$. $N = 4$ animals, $\alpha = 0.05$.

Alpha-smooth muscle actin (αSMA) labels vascular smooth muscle cells present within arteries, arterioles and pericytes. In contrast to the other cell markers, αSMA-positive staining (Figure 5A) increased along blood vessel structures in the cortex between DIV0 and DIV3 and DIV7. Image analysis revealed a significant increase in αSMA mean pixel value per unit area from 1.1×10^{-6} at DIV0 to 2.4×10^{-6} at DIV7 ($P = 0.0061$) (Figure 5B). Finally, rat endothelial cell antigen 1 (RECA-1) staining, which recognizes a cell surface antigen on endothelial cells, showed a reduction in staining of small vessels and capillaries at DIV3 and 7 (Figure 5C). Image analysis (Figure 5D) showed a marked and significant reduction in mean RECA-1 pixel value per unit area in the cortex, falling from 5.4×10^{-6} at DIV0 to 1.9×10^{-6} and 1.8×10^{-6} at DIV3 and DIV7 respectively ($P = 0.0003$ for both). A similar outcome was shown in the deeper tissues in proximity to the basal ganglia (Figure S4).

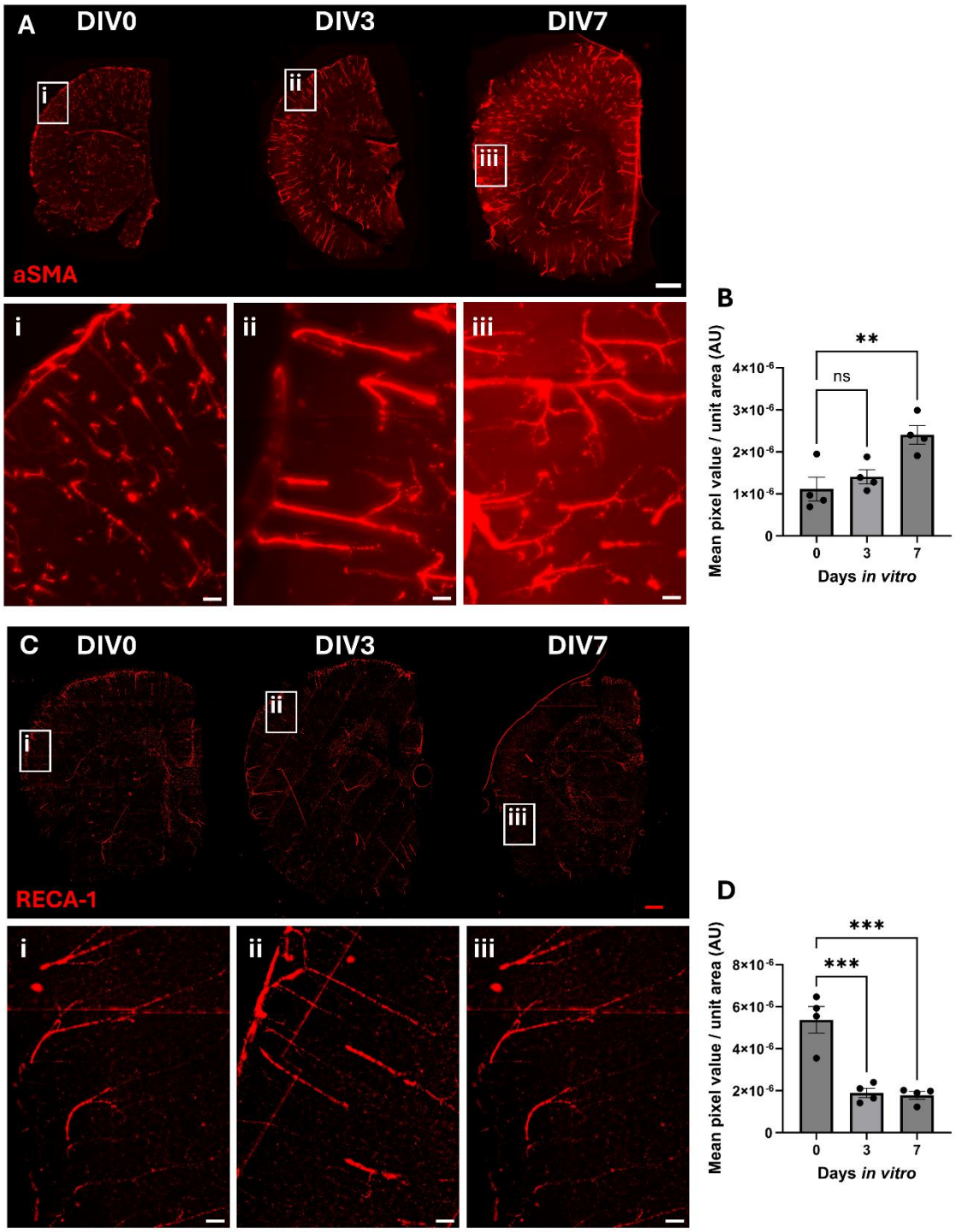

Figure 5 - Immunofluorescent staining of smooth muscle cells, pericytes and endothelial cells in OBSCs after 0, 3 and 7 days *in* vitro (DIV). Representative immunofluorescent staining of A) αSMA (alpha smooth muscle actin) and C) rat endothelial cell antigen 1 (RECA-1) shown in red (scale bars = 1,000 µm). Magnified regions of the cortex of section are shown in insets 'i', 'ii' and 'iii' for DIV0, 3 and 7 respectively (scale bars = 100 µm in insets), in addition to quantification of the mean pixel value per unit area for these regions B) αSMA quantification, D) RECA1 quantification. Each datapoint is mean of 3 regions of interest per brain slice, ±SEM. All statistics were performed with one-way ANOVA with

Dunnett's multiple comparisons test (all to control). ns = not significant, ** $P < 0.01$, *** $P < 0.001$, **** $P < 0.0001$. $N = 4$ animals, $\alpha = 0.05$.

4.3. Blood exposure induced increases in fibronectin and collagen deposits in OBSCs

OBSCs were exposed to lysed blood for 6, 24 or 48 hours to mimic haemorrhagic stroke, initiated at either DIV0 (acute) or DIV7 (7-day preculture). Fibronectin staining was shown to be minimal in acute sections (Figure 6A), with image analysis in the cortex and subcortical white matter (Figure 6B and Figure S8, respectively), and Western blotting of cortical protein isolates (Figure 6C and D) showing no significant increase in fibronectin staining or expression at any timepoint ($P > 0.05$ for all). However, control OBSCs cultured for 7 days showed visually greater fibronectin staining (Figure 6E) compared to acute sections (Figure 6A). Exposure of these pre-cultured OBSCs to blood resulted in a significant, near 10-fold increase in cortical vessels co-locating with fibronectin, from a mean of 2.97% in control OBSCs to a mean of 28.61% following blood exposure for 48 hours ($P = 0.0123$) (Figure 6F). This was further evidenced by a significant increase in fibronectin protein expression as assessed by Western blot, increasing 2.27-fold following blood exposure ($P = 0.038$) (Figure 6G and H). No significant change was noted in fibronectin staining in the subcortical white matter (Figure S8).

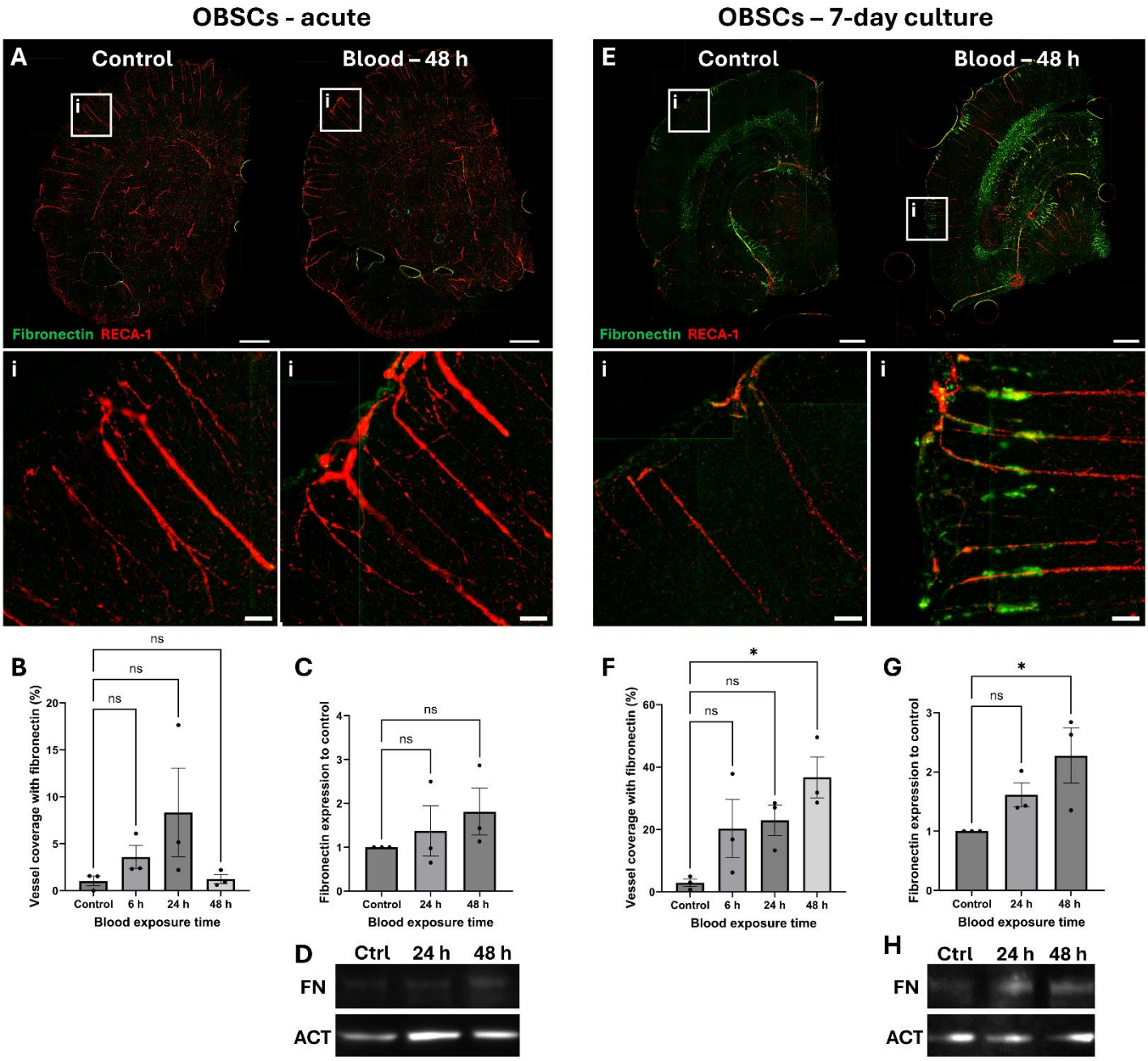

Figure 6 – Localisation and quantification of fibronectin in blood-exposed OBSCs. OBSCs were generated and cultured either for 0 or 7 days, after which they were exposed either to PBS (control) or the same volume of lysed blood for 48 hours. OBSCs were then fixed and stained for RECA1 (red) and fibronectin (green). Representative images of whole hemispheres are shown (A – acute, E – 7 day pre-cultured, scale bars = 1,000 µm). Insets show magnified regions of the cortex (i) (scale bars = 100 µm). Quantification of the percentage coverage of fibronectin on RECA1-stained vessels was performed (B, F). Fibronectin protein expression at 24 and 48 hours of blood exposure was also assessed by Western blot (D, H), followed by quantification of fibronectin fold-change (C, G). Each image quantification datapoint is the mean of three regions of interest from one brain slice per animal, ± SEM. All statistics were performed with one-way ANOVA with Dunnett's multiple comparisons test (all to control). ns = not significant, $N = 3$ animals, $\alpha = 0.05$.

A similar outcome was noted in the staining and expression of collagen IV, with acute OBSCs showing a significant increase in cortical vessel coverage from 1.55% in control samples to 16.15% after 24 hours of blood exposure ($P = 0.0491$, Figure 7B). No significant difference was seen in collagen IV staining in the white matter ($P > 0.05$ for all, Figure S8). In contrast to acute cultures, OBSCs treated with blood at DIV7 generated a marked increase in collagen IV signal, increasing from 7.92% cortical vessel coverage by collagen IV in the control to 32.84% after blood exposure ($P = 0.0032$, Figure 7D).

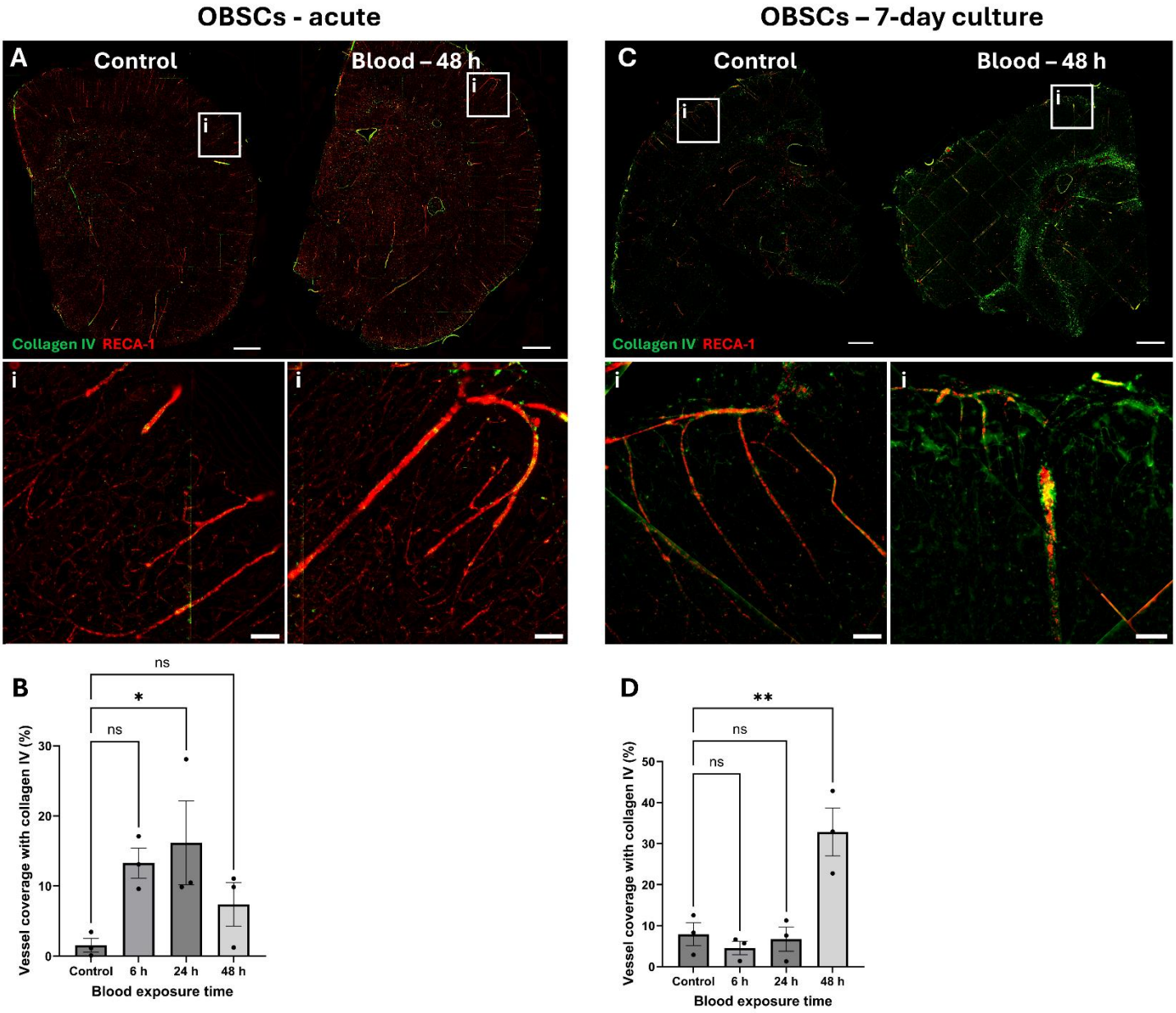

Figure 7 - Localisation and quantification of collagen IV in blood-exposed OBSCs. OBSCs were generated and cultured either for 0 or 7 days, after which they were exposed either to PBS (control) or the same volume of lysed blood for 48 hours. OBSCs were then fixed and stained for RECA1 (red) and collagen IV (green). Representative images of whole hemispheres are shown (A – acute, C – 7 day pre-cultured, scale bars = 1,000 µm). Insets show magnified regions of the cortex (i) (scale bars = 100 µm). Quantification of the percentage coverage of collagen IV on RECA1-stained vessels was performed (B, D). Each image quantification datapoint is the mean of three regions of interest from one brain slice per animal, ± SEM. All statistics were performed with one-way ANOVA with Dunnett's multiple comparisons test (all to control). ns = not significant, $N = 3$ animals, $\alpha = 0.05$.

385 **4.4. RNA-sequencing of blood-exposed OBSCs**

386 Following sample quality control and principal component analysis (supplementary materials
387 Figure S1 and S2), one blood-treated sample (B1) was excluded due to sequencing of an
388 insufficient sample quality leading to poor mapping to the reference genome. All subsequent
389 analysis was performed without this sample. Volcano plots were generated for all
390 differentially expressed genes (DEGs) ($pAdj < 0.05$) with expression fold changes (FC) > 2,
391 (Figure 8A) and greater than 1.5 (Figure 8B), with 95 and 604 DEGs over this FC cutoff,
392 respectively. Heatmaps were also generated for each sample across the 25 most upregulated
393 and 25 most downregulated DEGs (Figure 8C).

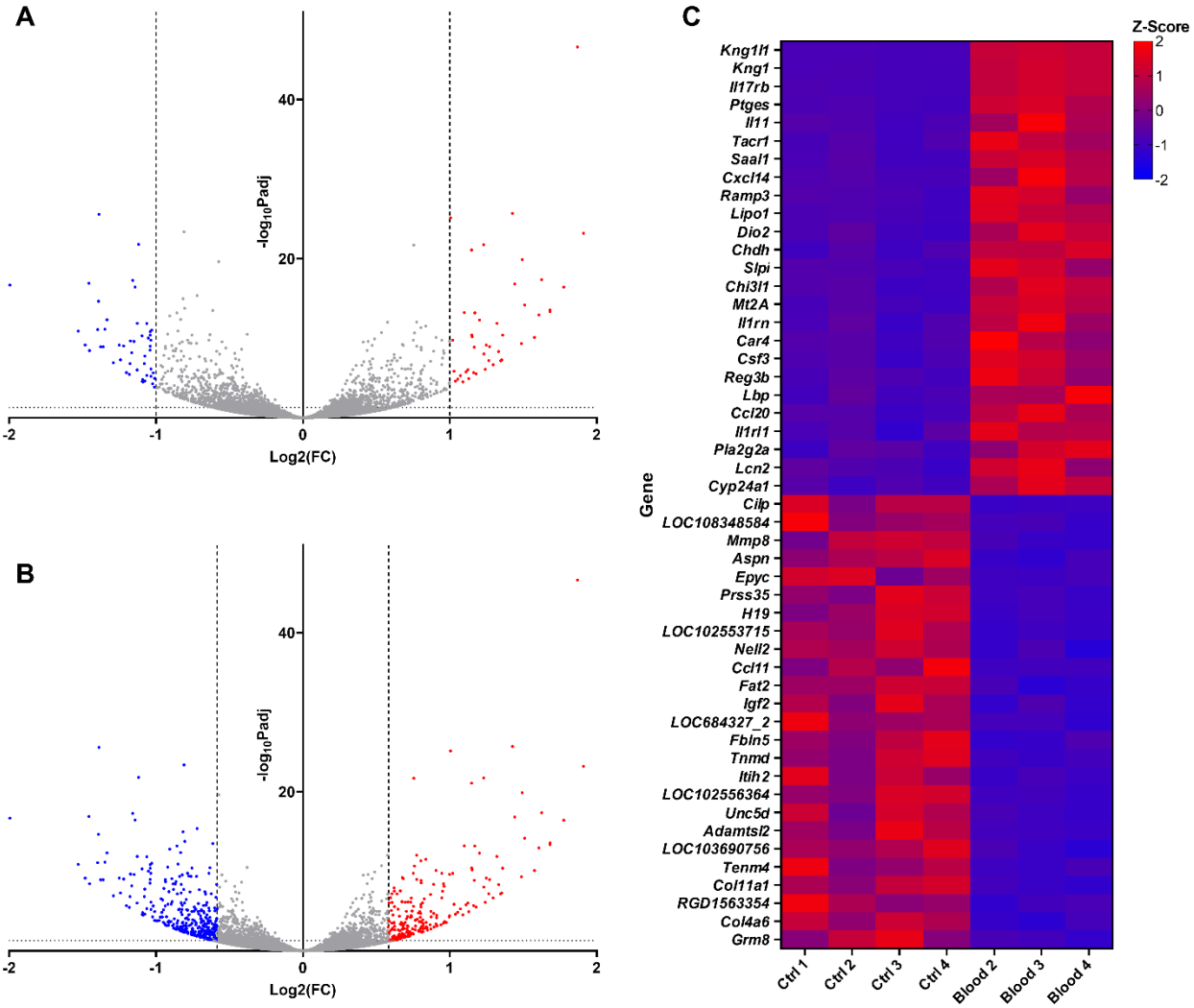

Figure 8 - Volcano plots and heatmap of top 25 most differentially expressed genes (DEGs) in control and blood-treated OBSCs. Volcano plots set with a fold change threshold >2 (A) and >1.5 (B) (with fold change thresholds depicted by dotted vertical lines), showing upregulated DEGs (*pAdj* < 0.05) in red and downregulated DEGs in blue. Z-scores for top 25 most up- and down-regulated DEGs (ranked by $\log_2$ fold change) are visualised via heatmap (C), with upregulated genes shown in red and downregulated genes in blue.

RT-qPCR validation of the top 6 most upregulated and downregulated genes (Figure 9) showed a significant decrease in *Aspn*, *Epyc*, *H19*, *Mmp8* and *Prss35* transcript expression after blood exposure (P = 0.0107, 0.0159, 0.0027, 0.026 and 0.0297 respectively. There was no significant reduction in *Cilp* expression, likely due to high inter-sample variability (P = 0.2207). Inversely, a significant upregulation of *Il11*, *Ptges* and *Saal1* was shown (P =

<0.0001, 0.0015 and 0.0006 respectively). Increases in *Kng1*, *Il17rb* and *Tacr* were not significant (P = 0.1307, 0.1109 and 0.0667). Overall, 8 of the 12 tested genes showed a significant change in expression (66.7%), with all showing a trend in the same direction as RNA-sequencing data following blood exposure.

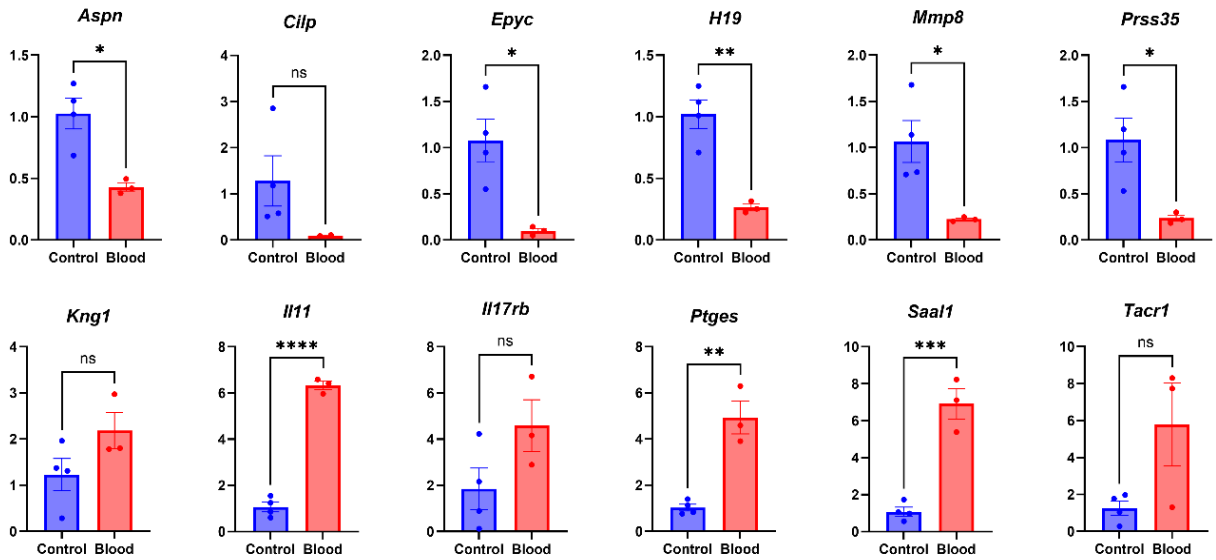

Figure 9 - RT-qPCR validation of RNA-sequencing. Top 6 downregulated (lower expression in blood-exposed samples) and top 6 upregulated (higher expression in blood-exposed samples). All statistical analyses were performed with unpaired t-tests. ns = not significant, ns = not significant, * P < 0.05, ** P < 0.01, *** P < 0.001, **** P < 0.0001, N = 3, α = 0.05.

Gene ontology (GO) analysis was then performed across cellular component (CC), biological process (BP) and molecular function (MF) GO families. Within the CC family (Figure 10A), 'extracellular region' and 'extracellular matrix' were the top two most over-represented GO terms (gene ratios 0.137 and 0.285, *padj* 6.45×10^{-29} and 8.96×10^{-27} respectively). DEGs from extracellular region (Figure 10B) and extracellular matrix terms (Figure 10C) showed downregulation in blood-treated OBSCs including *Col11a1*, *Col4a6* and *Eln*, downregulation of *Mmp8* and upregulation of *Mmp9*, *Mmp3* and *Timp1*.

424 'Response to external stimulus' and 'response to chemical' were the top two most over-
425 represented terms within the BP family (Figure 10D). 'Inflammatory response' and 'response
426 to oxidative stress' were selected for display (gene ratios 0.141 and 0.149, *padj* 9.64×10^{-11}
427 and 1.06×10^{-7} respectively), with DEGs from these terms shown in Figure 10E and F
428 respectively. Blood exposure appeared to cause a marked upregulation of included cytokines
429 and cytokine receptors, including *Ccl20*, *Il1rn*, *Il1r1* and *Il17rb*.

430 In the MF family, 'glycosaminoglycan binding' and 'signalling receptor binding' were the
431 topmost over-represented terms (Figure 10G). 'Signalling receptor binding' and 'cytokine
432 activity' were selected for display (gene ratios 0.129 and 0.168, *padj* 6.55×10^{-10} and $5.85 \times 10^{-}$
433 ^{5}), with DEGs from these terms shown in Figure 10H and Figure 10I, respectively. Blood
434 exposure led to an increase in expression of *Il11*, *Csf3*, *Fgf7* and *Lbp* and a downregulation in
435 *Igf2* and *Fbln5*, as examples.

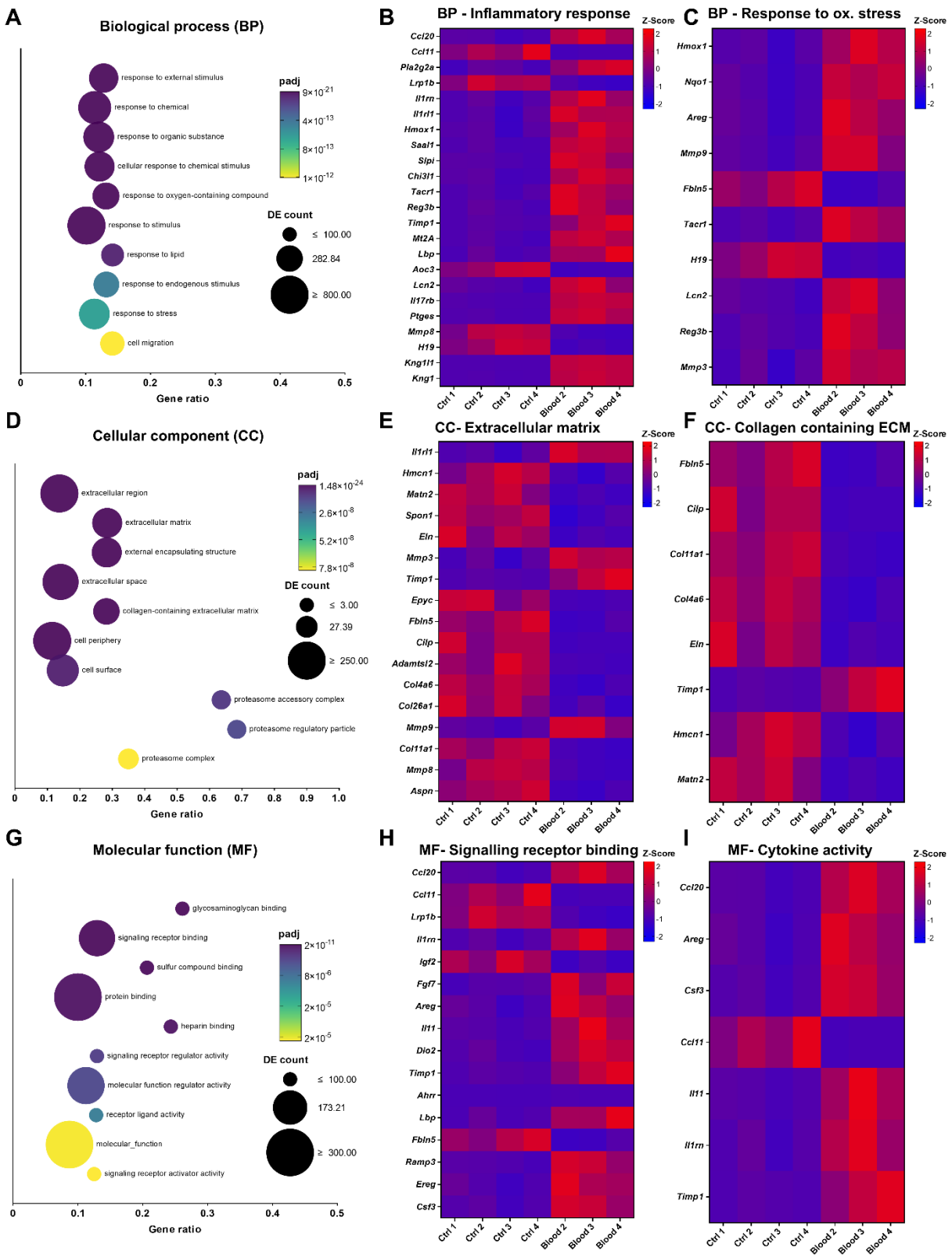

Figure 10 – Gene ontology (GO) for control and blood-treated OBSC, with DEGs from selected GO terms within each family. A, D, G) Biological process, cellular component and molecular function GO families depicted with the top 10 most significant overrepresented CC GO terms shown as a bubble plot. The colour scale depicts adjusted p-value (*padj*) and

441 bubble size represents the number of differentially expressed genes included in the respective
442 category. Gene ratio of 1 = all genes in the GO category are DE, whilst 0 = none. B, C, E, F,
443 H, I) Heatmaps of Z-score of DEGs with FC>2 or <0.5 within selected significantly over-
444 represented GO terms 'inflammatory response', 'response to oxidative stress', 'extracellular
445 matrix', 'collagen containing extracellular matrix', 'signalling receptor binding' and
446 'cytokine activity' respectively.
447

448

449 ## 5. Discussion

450 We have described an approach to the generation of adult rat OBSCs and their novel
451 application to the development of an *ex vivo* haemorrhagic stroke model. We demonstrate that
452 blood products have direct effects on ECM regulation in cortical blood vessels at both the
453 transcript and protein level. In addition, we have characterised the distribution and number of
454 several key brain cell types (neurons, endothelial cells, arterial smooth muscle/pericytes,
455 astrocytes and microglia) after 0, 3 and 7 days in culture. All cell types were present across
456 the measured time-course but showed differences in their response to culture conditions.

457 No significant change was noted in NeuN-positive cell staining, suggesting neurons were not
458 substantially impacted by the length of time in culture. In contrast, there was a significant
459 reduction in cortical GFAP-positive cells, particularly in the glia limitans, observed between
460 DIV0 and DIV3/7. This could be due to either loss of astrocytes or reduction in GFAP
461 expression within astrocytes. The latter seems plausible as the mechanical injury caused by
462 vibratome sectioning has been shown to cause glial cell activation, a hallmark of which is
463 GFAP upregulation [23,24]. The reduction in GFAP levels observed in our study could therefore
464 represent the return of GFAP to resting levels following an initial slicing-induced spike [25].
465 Quantification of astrocyte number is required to confirm this idea, but if correct, this
466 interpretation would support the rationale for culturing brain slices for longer periods of time
467 [13] before initiating studies in these models. Interestingly, GFAP levels were not reduced
468 everywhere in the brain slice, and GFAP-positive staining was maintained over the time-

course within the subcortical white matter. IBA1-positive microglia in the cortex also reduced from DIV0 to DIV3/7. Delbridge *et al*., reported a reduction in microglial proliferation and an increase in microglial inflammation in the days following slice preparation [26], likely leading to the observed fall in microglia numbers seen here.

We did observe a significant reduction in RECA-1 staining, particularly associated with capillaries, suggesting a loss of endothelial cells (ECs) from the OBSCs. We suggest that the lack of blood flow, and thus the lack of a pulsatile hemodynamic force and shear stress experienced by the ECs [27], contributes to this loss. Previous studies have shown that decreased blood flow directly affects EC migration and cytoskeleton reorganisation [28], and causes apoptosis and a reduction in EC number in previously dilated arteries [29]. Alternatively, our data could be explained by a reduction in the abundance of the RECA-1 epitope (an unknown protein) within endothelial cells which has been suggested by Moser and colleagues [30]. At the same time, an increase in αSMA-positive cells was seen at DIV 7, suggesting a rise in the number of arterial smooth muscle cells (SMCs) or pericytes. Previous studies show a causative link between reduced blood flow and disordered vascular remodelling [31] and increased SMC proliferation (shown initially in hypertensive models) [32].

CCP3 staining increased between DIV0 and DIV3/7, indicating an increase in apoptosis-driven cell death, which is to be expected due to the acclimatisation of slices to culture following the injurious process of vibratome sectioning. This finding does suggest a possible upper limit to the culture period, though longer culture durations were not tested in the present work. Overall, these data suggest the successful maintenance of most tested cell types in OBSCs, with a possible degradation in blood vessel endothelium due to a lack of blood flow through the vasculature. For this reason, future works employing this model (for example, studies of the blood brain barrier) may choose to employ a shorter pre-culture period, with the caveat of increased astrogliosis and inflammation.

494 Following this, adult rat OBSCs were cultured for 0 and 7 days and then exposed to lysed rat
495 blood for 6, 24 or 48 hours to mimic haemorrhagic stroke. Two key markers of fibrosis,
496 fibronectin [33,34] and collagen IV [35,36],were both significantly elevated along cortical blood
497 vessels (as measured by immunostaining) only in the 7-day cultures. 48 hours of blood
498 exposure generated the largest response, both on immunofluorescent stains and Western blots.
499 Our results show that these fibrotic deposits are primarily localised to penetrating cortical
500 vessels, where αSMA is most prominent. Interestingly, these deposits were not observed in
501 the 0-day cultures where there were lower levels of αSMA. This potentially indicating the
502 involvement of SMCs or pericytes in modulating ECM associated with blood vessels. The
503 location of ECM deposits suggest they could contribute to disordered glymphatic flow,
504 reducing the clearance of metabolites (and blood products following haemorrhagic stroke)
505 and exacerbating brain injury. Indeed, perivascular fibrosis has previously been reported in
506 *in vivo* models of ICH [37,38] and SAH [39] and directly linked to reduced clearance of amyloid-β
507 after ischemic stroke [40].

508 In addition to immunostaining and Western blotting, RNA sequencing was performed on
509 RNA isolated from 7-day precultured OBSCs exposed to blood for 48 hours. Blood exposure
510 led to significant over-expression of inflammatory response and cytokine signalling related
511 GO terms, driven by a marked upregulation of inflammation-linked genes, including *Ccl20*,
512 *Il11* and *Csf3*. *Ccl20* has previously been linked to neuroinflammation following traumatic
513 brain injury [41] with antagonism shown to reduce this following SAH [42]. *Il11* concentration in
514 plasma post-ICH has been shown to positively correlate with increased mortality and the
515 development of hydrocephalus [43]. *Il11* has also been linked to inflammatory immune cell
516 migration in multiple sclerosis [44] and protection against ischemia reperfusion injury in middle
517 cerebral artery occlusion (MCAO) models of ischemic stroke [45]. *Csf3* has been suggested to
518 play a role in post-MCAO brain injury by increasing neutrophil toxicity [46]. This large drive

519 towards a pro-inflammatory transcriptome following blood exposure supports studies
520 examining the pro-inflammatory nature of blood and blood products in the subarachnoid
521 space and parenchyma following haemorrhagic stroke [47,48] and suggests that this crucial
522 element is successfully recapitulated in our OBSC-based haemorrhagic stroke model.

523 Interestingly, the same RNA sequencing data showed a downregulation of ECM-related GO
524 terms and genes (including collagens and elastin), with some upregulation of matrix
525 metalloproteinases (MMPs) and tissue inhibitors of metalloproteinases (TIMPs).
526 Immunofluorescent staining and Western blotting of blood-exposed OBSCs suggested a
527 marked increase in ECM deposition along cortical vessels, as previously discussed,
528 suggesting a differential response at the gene and protein level. We propose this increase in
529 protein deposition may not be due to changes in *de novo* protein synthesis, but a manipulation
530 of ECM turnover triggered by blood-induced changes in the expression of MMPs and TIMPs.
531 Indeed, modified *Mmp9*/*Timp1* expression (as shown in our RNA sequencing data) has been
532 linked to disordered collagen deposition in the skin [49] and lung [50]. In the brain, a reduction in
533 collagen IV RNA and upregulation of *Mmp9* has previously been reported 48 hours after
534 SAH [51], a finding reflected in the present work. These findings suggest that our model also
535 successfully mimics the ECM dysfunction seen in haemorrhagic stroke, with a likely
536 breakdown of the blood brain barrier and disordered, fibrotic ECM deposition along cortical
537 penetrating vessels.

538 A limitation of our model is that it simulates global blood exposure instead of localised blood
539 exposure to the cortical tissues or ventricles (as may be seen after SAH or IVH). Further
540 work may be undertaken to identify if this model can recapitulate the differences seen
541 between types of haemorrhagic stroke, i.e SAH and ICH [8]. Single cell RNA sequencing may
542 also determine which cells drive fibrosis following blood exposure, as the mechanism
543 underlying this has not been explored in the present work.

Our findings suggest that our OBSC model can a) successfully maintain adult rat brain slices for at least 7 days and b) employ lysed blood to recapitulate the disordered ECM deposition (fibrosis) and neuroinflammation which follows haemorrhagic stroke. Future studies may employ this model to further understand the molecular drivers of post-stroke inflammation and fibrosis, or to trial anti-fibrotic agents to reduce ECM dysfunction. Our model offers a platform to advance the translation of pharmacological treatments aimed at reducing post-stroke disability and improving outcomes for stroke survivors, whilst providing a higher throughput and physiologically realistic alternative to *in vivo* animal studies.

6. Declarations

6.1. Disclosures

PK and RMB are founders and shareholders in Estuar Pharmaceuticals. The other authors declare they have no financial and/or non-financial interests that may cause a conflict of interest.

6.2. Funding

This research was funded by a Medical Research Foundation grant (MRF-076-0002-RG-BOTF-C0754). LR was supported by a Midlands Integrative Biosciences Training Programme studentship (MIBTP, reference BB/T00746X/1) from the Biotechnology and Biological Sciences Research Council (BBSRC). PK is supported by a BBSRC Discovery Fellowship (BB/W00934X/1). RMB is supported by a UKRI Frontier Research Grant EP/Y023684/1 (following assessment as an ERC Advanced grant, FORTIFY, ERC-2022-ADG-101096882 under the UK Government Guarantee scheme) and acknowledges a Biotechnology and Biological Sciences Research Council Pioneer Award (BB/Y512874/1).

566 **6.3. Data availability**

567 RNA sequencing data have been uploaded to the NCBI sequence read archive (SRA) and are
568 freely available for use (BioProject ID PRJNA1262501). Uncropped, unedited Western blots
569 are included in the supplemental materials (Figures S3 and S4). Image quantification macros
570 are available (supplemental materials, 'ImageJ macro language scripts used for image
571 quantification'). All other data will be made available upon request to the corresponding
572 authors.

573 **6.4. Authors' contributions (CRediT)**

574 BJH: methodology, software, formal analysis, resources, investigation, data curation, writing
575 – original draft, visualisation. LR: investigation, data curation, writing – review and editing.
576 JAR: formal analysis, writing – review and editing. DF: resources, writing – review and
577 editing. PK: supervision, writing – review and editing. RMB: supervision, writing – review
578 and editing. LJH: supervision, writing – review and editing. HB: resources, writing – review
579 and editing, supervision, project administration, funding acquisition.

580 **7. Acknowledgements**

581 The authors thank the members of the Neuro-Ocular Inflammation and Matrix Research
582 Group (University of Birmingham) for their support and University of Birmingham
583 Biomedical Services Unit staff for their expert assistance in caring for the experimental
584 animals. We acknowledge the support of the Microscopy Technology Hub Facilities at the
585 College of Medicine and Health, University of Birmingham, for providing access to
586 equipment and technical expertise and the Birmingham Environment for Academic Research
587 (BEAR) advanced research computing team for use of high-performance computing services
588 and storage.

The Galaxy server used for some calculations is partly funded by the German Federal Ministry of Education and Research BMBF grant 031 A538A de.NBI-RBC and the Ministry of Science, Research and the Arts Baden-Württemberg (MWK) within the framework of LIBIS/de.NBI Freiburg. The Aston Institute for Membrane Excellence (AIME) is funded by UKRI's Research England as part of their Expanding Excellence in England (E3) fund.

8. References

1. Donkor ES. Stroke in the 21st Century: A Snapshot of the Burden, Epidemiology, and Quality of Life. *Stroke Res Treat*. 2018;2018:1–10.

2. Waziry R, Heshmatollah A, Bos D, Chibnik LB, Ikram MA, Hofman A, Ikram MK. Time Trends in Survival Following First Hemorrhagic or Ischemic Stroke Between 1991 and 2015 in the Rotterdam Study. *Stroke*. 2020;51:824–829.

3. Lauzier DC, Jayaraman K, Yuan JY, Diwan D, Vellimana AK, Osbun JW, Chatterjee AR, Athiraman U, Dhar R, Zipfel GJ. Early Brain Injury After Subarachnoid Hemorrhage: Incidence and Mechanisms. *Stroke*. 2023;54:1426–1440.

4. Hu Z, Deng X, Zhou S, Zhou C, Shen M, Gao X, Huang Y. Pathogenic mechanisms and therapeutic implications of extracellular matrix remodelling in cerebral vasospasm. *Fluids Barriers CNS*. 2023;20. doi:10.1186/S12987-023-00483-8,.

5. Douglas MR, Daniel M, Lagord C, Akinwunmi J, Jackowski A, Cooper C, Berry M, Logan A. High CSF transforming growth factor β levels after subarachnoid haemorrhage: association with chronic communicating hydrocephalus. *J Neurol Neurosurg Psychiatry*. 2009;80:545–550.

610 6. Chen S, Luo J, Reis C, Manaenko A, Zhang J. Hydrocephalus after Subarachnoid
611 Hemorrhage: Pathophysiology, Diagnosis, and Treatment. *Biomed Res Int*. 2017;2017.
612 doi:10.1155/2017/8584753,.

613 7. Motohashi O, Suzuki M, Shida N, Umezawa K, Ohtoh T, Sakurai Y, Yoshimoto T.
614 Subarachnoid haemorrhage induced proliferation of leptomeningeal cells and
615 deposition of extracellular matrices in the arachnoid granulations and subarachnoid
616 space - Immunhistochemical study. *Acta Neurochir (Wien)*. 1995;136:88–91.

617 8. Hewitt B, Ali M, Hubbard J, Hill L, Botfield H. A systematic review of the differential
618 effects of TGFβ-1 in ischemic and hemorrhagic pre-clinical stroke models. *J Am Heart*
619 *Assoc*. 2025.

620 9. LI CL, McILWAIN H. Maintenance of resting membrane potentials in slices of
621 mammalian cerebral cortex and other tissues in vitro. *J Physiol*. 1957;139:178.

622 10. Croft CL, Futch HS, Moore BD, Golde TE. Organotypic brain slice cultures to model
623 neurodegenerative proteinopathies. *Molecular neurodegeneration 2019 14:1*.
624 2019;14:1–11.

625 11. Eisemann T, Costa B, Strelau J, Mittelbronn M, Angel P, Peterziel H. An advanced
626 glioma cell invasion assay based on organotypic brain slice cultures. *BMC Cancer*.
627 2018;18:1–10.

628 12. Magalhães DM, Pereira N, Rombo DM, Beltrão-Cavacas C, Sebastião AM, Valente
629 CA. Ex vivo model of epilepsy in organotypic slices-a new tool for drug screening. *J*
630 *Neuroinflammation*. 2018;15:1–18.

631 13. Humpel C. Organotypic brain slice cultures: A review. *Neuroscience*. 2015;305:86–98.

632 14. Alaylioğlu M, Dursun E, Yilmazer S, Gezen Ak D. A Bridge Between in vitro and in
633 vivo Studies in Neuroscience: Organotypic Brain Slice Cultures. *Archives of*
634 *neuropsychiatry*. 2020;57:333.

635 15. Jacobs BS, Boden-Albala B, Lin IF, Sacco RL. Stroke in the young in the Northern
636 Manhattan stroke study. *Stroke*. 2002;33:2789–2793.

637 16. Mokrushin AA, Khama-Murad AX, Pavlinova LI. Effects of Long-Term Exposure of
638 Nerve Cells to Autoblood in In Vitro Model of Hemorrhagic Stroke. ; 2008: 1-355–
639 357.

640 17. Schindelin J, Arganda-Carreras I, Frise E, Kaynig V, Longair M, Pietzsch T, Preibisch
641 S, Rueden C, Saalfeld S, Schmid B, et al. Fiji: An open-source platform for biological-
642 image analysis. Nat Methods. . 2012;9:676–682.

643 18. Liao Y, Smyth GK, Shi W. featureCounts: an efficient general purpose program for
644 assigning sequence reads to genomic features. *Bioinformatics*. 2014;30:923–930.

645 19. Abueg LAL, Afgan E, Allart O, Awan AH, Bacon WA, Baker D, Bassetti M, Batut B,
646 Bernt M, Blankenberg D, et al. The Galaxy platform for accessible, reproducible, and
647 collaborative data analyses: 2024 update. *Nucleic Acids Res*. 2024;52:W83–W94.

648 20. Ewels P, Magnusson M, Lundin S, Käller M. MultiQC: summarize analysis results for
649 multiple tools and samples in a single report. *Bioinformatics*. 2016;32:3047–3048.

650 21. Love MI, Huber W, Anders S. Moderated estimation of fold change and dispersion for
651 RNA-seq data with DESeq2. *Genome Biol*. 2014;15:1–21.

652 22. Young MD, Wakefield MJ, Smyth GK, Oshlack A. Gene ontology analysis for RNA-
653 seq: accounting for selection bias. *Genome Biol*. 2010;11:1–12.

654 23. Pekny M, Pekna M. Astrocyte reactivity and reactive astrogliosis: Costs and benefits.
655 *Physiol Rev*. 2014;94:1077–1098.

656 24. Stence N, Waite M, Dailey ME. Dynamics of microglial activation: A confocal time-
657 lapse analysis in hippocampal slices. *Glia*. 2001;33:256–266.

658 25. Humpel C. Long-term live-cell imaging of GFAP+ astroglia and laminin+ vessels in
659 organotypic mouse brain slices using microcontact printing. *Front Cell Neurosci*.
660 2025;19:1540150.

661 26. Delbridge ARD, Huh D, Brickelmaier M, Burns JC, Roberts C, Challa R, Raymond N,
662 Cullen P, Carlile TM, Ennis KA, et al. Organotypic Brain Slice Culture Microglia
663 Exhibit Molecular Similarity to Acutely-Isolated Adult Microglia and Provide a
664 Platform to Study Neuroinflammation. *Front Cell Neurosci*. 2020;14:592005.

665 27. Li YSJ, Haga JH, Chien S. Molecular basis of the effects of shear stress on vascular
666 endothelial cells. *J Biomech*. 2005;38:1949–1971.

667 28. Vyalov S, Langille BL, Gotlieb AI. Decreased blood flow rate disrupts endothelial
668 repair in vivo. *Am J Pathol*. 1996;149:2107.

669 29. Sho E, Sho M, Singh TM, Xu C, Zarins CK, Masuda H. Blood flow decrease induces
670 apoptosis of endothelial cells in previously dilated arteries resulting from chronic high
671 blood flow. *Arterioscler Thromb Vasc Biol*. 2001;21:1139–1145.

672 30. Moser K V., Schmidt-Kastner R, Hinterhuber H, Humpel C. Brain capillaries and
673 cholinergic neurons persist in organotypic brain slices in the absence of blood flow.
674 *European journal of neuroscience*. 2003;18:85–94.

675 31. Ward MR, Tsao PS, Agrotis A, Dilley RJ, Jennings GL, Bobik A. Low blood flow after
676 angioplasty augments mechanisms of restenosis: inward vessel remodeling, cell

677 migration, and activity of genes regulating migration. *Arterioscler Thromb Vasc Biol*.
678 2001;21:208–213.

679 32. Ueno H, Kanellakis P, Agrotis A, Bobik A. Blood flow regulates the development of
680 vascular hypertrophy, smooth muscle cell proliferation, and endothelial cell nitric
681 oxide synthase in hypertension. *Hypertension*. 2000;36:89–96.

682 33. Andrews RN, Caudell DL, Metheny-Barlow LJ, Peiffer AM, Tooze JA, Bourland JD,
683 Hampson RE, Deadwyler SA, Cline JM. Fibronectin Produced by Cerebral Endothelial
684 and Vascular Smooth Muscle Cells Contributes to Perivascular Extracellular Matrix in
685 Late-Delayed Radiation-Induced Brain Injury. *Radiat Res*. 2018;190:361–373.

686 34. Altrock E, Sens C, Wuerfel C, Vasel M, Kawelke N, Dooley S, Sottile J, Nakchbandi
687 IA. Inhibition of fibronectin deposition improves experimental liver fibrosis. *J*
688 *Hepatol*. 2015;62:625–633.

689 35. Stichel CC, Hermanns S, Luhmann HJ, Lausberg F, Niermann H, D'Urso D, Servos G,
690 Hartwig H-G, Müller HW. Inhibition of collagen IV deposition promotes regeneration
691 of injured CNS axons. *European journal of neuroscience*. 1999;11:632–646.

692 36. Klapka N, Hermanns S, Straten G, Masanneck C, Duis S, Hamers FPT, Müller D,
693 Zuschratter W, Müller HW. Suppression of fibrous scarring in spinal cord injury of rat
694 promotes long-distance regeneration of corticospinal tract axons, rescue of primary
695 motoneurons in somatosensory cortex and significant functional recovery. *Eur J*
696 *Neurosci*. 2005;22:3047–3058.

697 37. Li H, Ghorbani S, Ling CC, Yong VW, Xue M. The extracellular matrix as modifier of
698 neuroinflammation and recovery in ischemic stroke and intracerebral hemorrhage.
699 *Neurobiol Dis*. 2023;186. doi:10.1016/j.nbd.2023.106282.

700 38. Li H, Ghorbani S, Zhang R, Ebacher V, Stephenson EL, Keough MB, Yong VW, Xue
701 M. Prominent elevation of extracellular matrix molecules in intracerebral hemorrhage.
702 *Front Mol Neurosci*. 2023;16:1251432.

703 39. Macdonald RL, Weir BKA, Young JD, Grace MGA. Cytoskeletal and extracellular
704 matrix proteins in cerebral arteries following subarachnoid hemorrhage in monkeys. *J*
705 *Neurosurg*. 1992;76:81–90.

706 40. Howe M. The Role Of Perivascular Fibrosis In Post-Stroke Glymphatic Impairment
707 And Cerebral Amyloid Angiopathy. *Dissertations & theses (open access)*. 2018.
708 Available at https://digitalcommons.library.tmc.edu/utgsbs_dissertations/875. Accessed
709 February 28, 2025.

710 41. Das M, Leonardo CC, Rangooni S, Mohapatra SS, Mohapatra S, Pennypacker KR.
711 Lateral fluid percussion injury of the brain induces CCL20 inflammatory chemokine
712 expression in rats. *J Neuroinflammation*. 2011;8:1–16.

713 42. Liao LS, Zhang MW, Gu YJ, Sun XC. Targeting CCL20 inhibits subarachnoid
714 hemorrhage-related neuroinflammation in mice. *Aging*. 2020;12:14849–14862.

715 43. Fang HY, Ko WJ, Lin CY. Plasma interleukin 11 levels correlate with outcome of
716 spontaneous intracerebral hemorrhage. *Surg Neurol*. 2005;64:511–517.

717 44. Seyedsadr M, Wang Y, Elzoheiry M, Gopal SS, Jang S, Duran G, Chervoneva I,
718 Kasimoglou E, Wrobel JA, Hwang D, et al. IL-11 induces NLRP3 inflammasome
719 activation in monocytes and inflammatory cell migration to the central nervous system.
720 *Proc Natl Acad Sci U S A*. 2023;120:e2221007120.

45. Zhang B, Zhang HX, Shi ST, Bai YL, Zhe X, Zhang SJ, Li YJ. Interleukin-11 treatment protected against cerebral ischemia/reperfusion injury. *Biomedicine & pharmacotherapy*. 2019;115:108816.

46. Garcia-Bonilla L, Racchumi G, Murphy M, Anrather J, Iadecola C. Endothelial CD36 Contributes to Postischemic Brain Injury by Promoting Neutrophil Activation via CSF3. *Journal of neuroscience*. 2015;35:14783–14793.

47. Madangarli N, Bonsack F, Dasari R, Sukumari–Ramesh S. Intracerebral Hemorrhage: Blood Components and Neurotoxicity. *Brain Sci*. 2019;9:316.

48. Alsbrook DL, Di Napoli M, Bhatia K, Biller J, Andalib S, Hinduja A, Rodrigues R, Rodriguez M, Sabbagh SY, Selim M, et al. Neuroinflammation in Acute Ischemic and Hemorrhagic Stroke. *Curr Neurol Neurosci Rep*. 2023;23:407–431.

49. Zhou P, Yang C, Zhang S, Ke ZX, Chen DX, Li YQ, Li Q. The Imbalance of MMP-2/TIMP-2 and MMP-9/TIMP-1 Contributes to Collagen Deposition Disorder in Diabetic Non-Injured Skin. *Front Endocrinol (Lausanne)*. 2021;12:734485.

50. Chen G, Ge D, Zhu B, Shi H, Ma Q. Upregulation of matrix metalloproteinase 9 (MMP9)/tissue inhibitor of metalloproteinase 1 (TIMP1) and MMP2/TIMP2 ratios may be involved in lipopolysaccharide-induced acute lung injury. *J Int Med Res*. 2020;48:0300060520919592.

51. Solár P, Zamani A, Lakatosová K, Joukal M. The blood–brain barrier and the neurovascular unit in subarachnoid hemorrhage: molecular events and potential treatments. *Fluids and barriers of the cns 2022 19:1*. 2022;19:1–79.